PHYSICAL REVIEW C **97**, 024319 (2018)

Rotational motion of triaxially deformed nuclei studied by the microscopic angular-momentum-projection method. II. Chiral doublet band

Mitsuhiro Shimada, Yudai Fujioka, Shingo Tagami, and Yoshifumi R. Shimizu
Department of Physics, Graduate School of Science, Kyushu University, Fukuoka 819-0395, Japan

(Received 29 November 2017; published 16 February 2018)

In the sequel of the present study, we have investigated the rotational motion of triaxially deformed nucleus by using the microscopic framework of angular-momentum projection. The Woods-Saxon potential and the schematic separable-type interaction are employed as a microscopic Hamiltonian. As the first example, nuclear wobbling motion was studied in detail in part I of the series. This second part reports on another interesting rotational mode, chiral doublet bands: two prototype examples, ^{128}Cs and ^{104}Rh, are investigated. It is demonstrated that the doublet bands naturally appear as a result of the calculation in this fully microscopic framework without any kind of core, and they have the characteristic properties of the $B(E2)$ and $B(M1)$ transition probabilities, which are expected from the phenomenological triaxial particle-rotor coupling model.

DOI: 10.1103/PhysRevC.97.024319

I. INTRODUCTION

It has been an interesting subject to study the rotational motion of triaxially deformed nucleus in the field of nuclear structure [1]. Although the triaxial deformation is rarely realized in the ground state of nuclei [2], it is more frequently expected at high-spin states, see, e.g., Refs. [3–5] and references therein. When the nuclear mean field is triaxially deformed, collective rotation about all three principal axes is possible, and therefore the total angular-momentum vector may tilt away from either of three principal axes. Then the quantized rotational spectrum of the rigid rotor will emerge, which is called nuclear wobbling [1]. Such rotational bands have been sought for a long time and finally identified first in ^{163}Lu [6]; see, e.g., Refs. [7,8] for recent theoretical review articles. This wobbling motion has been investigated in the first part of the present study [9]; we refer to it as part I hereafter.

Another specific rotational motion expected in a triaxially deformed nucleus are the chiral doublet bands, predicted for the first time in Ref. [10], where the tilting of the angular-momentum vector is caused by other degrees of freedom than the collective rotation; see, e.g., Ref. [11] for a recent review. For an odd-odd nucleus, where both an odd proton particle and an odd neutron hole occupies a high-j intruder orbitals, as a typical example, the odd particle angular-momentum aligns along the short axis and the odd hole angular-momentum along the long axis, because such alignments maximize the overlap of the wave function of the aligned particle or hole with triaxial density distribution of the core. If the three moments of inertia of the core are in irrotational-like ordering, the collective angular-momentum aligns along the medium axis, which has the largest moment of inertia. For moderate high-spin states, where all three kinds of angular momenta are sizable, these three vectors are aplanar, and the chiral symmetry between the right- and left-handedness is broken in such a system. It is then expected that a pair of degenerate $\Delta I = 1$ rotational bands appear as a result of breaking this symmetry. In Ref. [12], it is discussed that characteristic patterns are expected for the electromagnetic transition rates, $B(E2)$ and $B(M1)$ in this prototype situation with broken chiral symmetry.

These interesting types of rotational motion characteristic for triaxially deformed nucleus have been investigated mainly by phenomenological models such as the triaxial-rotor [1] or the particle-hole coupled to triaxial-rotor [10]. Here we study such rotational motion by employing the fully microscopic framework, where the nuclear wave function is constructed from the triaxially deformed mean field and the broken rotational symmetry is recovered by angular-momentum projection; see, e.g., Ref. [13]. With the projection method, the regular rotational spectrum is naturally obtained. Full three-dimensional (3D) projection from the mean-field wave function should be performed for triaxially deformed nuclei, so that an efficient method is necessary. We have developed such a method in Ref. [14], and applied it to the study of nuclear tetrahedral deformation [15,16], the γ vibration [17], and the ground-state rotational bands [18,19] in rare-earth nuclei. In this second part of the present investigation we also employ the same method to study the chiral doublet band for the case where the prototype considered in Ref. [12] is realized.

It should be mentioned that chiral doublet bands have been studied by a similar microscopic approach, the triaxial projected shell model, for the first time in Ref. [20]; see Refs. [21,22] for recent review articles. The authors are successful to reproduce the experimental data. The purpose of the present work is not to reproduce the experimental data, but rather to understand how the chiral doublet bands appear and how the ideal chiral geometry reflects to the observable quantities such as the electromagnetic transition rates. We believe that such an investigation is meaningful for deeper comprehension of the rotational motion in the triaxially deformed nucleus from the microscopic viewpoint.

The paper is organized as follows. We briefly recapitulate our formulation in Sec. II, where only the necessary mathematical expressions for discussion of the present study are included.

The more detailed content is presented in part I [9]. Possible occurrence of the chiral doublet band and its properties of the electromagnetic transition probabilities are studied for ^{128}Cs and ^{104}Rh nuclei in Sec. III. Finally, the results of the present study are summarized in Sec. IV. Preliminary results were already published in Ref. [23].

II. BASIC FORMULATION

In the series of the present work, we study collective rotation of triaxially deformed nucleus with the microscopic angular-momentum-projection method. The quantum eigenstates of rotational band are obtained by

$$\left|\Psi^I_{M\alpha}\right\rangle = \sum_K g^I_{K,\alpha}\, \hat{P}^I_{MK}|\Phi\rangle \tag{1}$$

from the mean-field state $|\Phi\rangle$, where the angular-momentum projector is denoted by $\hat{P}^I_{MK}$ and the amplitude $g^I_{K,\alpha}$ is determined by the so-called Hill-Wheeler equation, see, e.g., Ref [13];

$$\sum_{K'} \mathcal{H}^I_{K,K'}\, g^I_{K',\alpha} = E^I_\alpha \sum_{K'} \mathcal{N}^I_{K,K'}\, g^I_{K',\alpha}, \tag{2}$$

with the definition of the Hamiltonian and norm kernels,

$$\begin{Bmatrix} \mathcal{H}^I_{K,K'} \\ \mathcal{N}^I_{K,K'} \end{Bmatrix} = \langle\Phi| \begin{Bmatrix} \hat{H} \\ 1 \end{Bmatrix} \hat{P}^I_{KK'}|\Phi\rangle. \tag{3}$$

To investigate how the interesting types of rotational motion appear and what kind of properties they have, it is preferable to be able to change the mean-field parameters, e.g., the deformation parameters, arbitrarily. Therefore, we employ a model Hamiltonian $\hat{H}$ composed of the phenomenological Woods-Saxon potential and the schematic separable-type interaction, which has been also utilized in Refs. [14,15]. Its precise form is given in part I and we will not repeat it here.

When the projected wave function in Eq. (1) is obtained, it is straightforward to calculate the electromagnetic transition probabilities [13]. No effective charge is used for the calculation of $B(E2)$ because the full model space is employed without any kind of core. The effective spin g factor of $0.7 \times g_{s,\text{free}}$ is adopted for both neutrons and protons for the calculation of $B(M1)$. In this way there is no ambiguity for the calculation of these transition probabilities.

The product-type mean-field wave function with the pairing correlations, $|\Phi\rangle$ in Eq. (1), is generated by the mean-field Hamiltonian $\hat{h}_{\text{mf}}$ composed of the deformed Woods-Saxon potential and the monopole-type pairing potential, where the pairing potential has the form factor of the derivative of the Woods-Saxon potential, see part I for details. The deformation in the body-fixed frame is specified with respect to the equipotential surface at the half depth for the Woods-Saxon potential with the usual radius parametrization,

$$R(\theta,\varphi) = R_0\, c_v(\{\alpha\}) \left[1 + \sum_{\lambda\mu} \alpha^*_{\lambda\mu} Y_{\lambda\mu}(\theta,\varphi)\right], \tag{4}$$

with the quantity $c_v(\{\alpha\})$ that guarantees the volume-conservation condition. In the present work, we employ $\lambda = 2$ and 4 deformations with the parameters (β_2,β_4,γ), where the so-called Lund convention [24] is used for the sign of triaxiality parameter γ, and therefore, for example, $\langle x^2\rangle < \langle y^2\rangle < \langle z^2\rangle$ for $0^\circ < \gamma < 60^\circ$. Here $\langle x^2\rangle$ etc. are abbreviated notations of $\langle \sum_{i=a}^A (x^2)_a\rangle$ etc., which will be also used in the following discussions.

It is worthwhile mentioning that the triaxiality parameter in the Woods-Saxon potential, $\gamma \equiv \gamma(\text{WS})$, and the corresponding parameter in the Nilsson potential, $\gamma(\text{Nils})$, are somewhat different from that of the density distribution for the mean-field state, $\gamma(\text{den})$, which is defined by

$$\gamma(\text{den}) \equiv \tan^{-1}\left[-\frac{\sqrt{2}\langle Q_{22}\rangle}{\langle Q_{20}\rangle}\right], \tag{5}$$

where $Q_{2\mu}$ is the quadrupole operator; see Ref. [25] for the precise definitions of the various γ parameters and discussion related to them. Although the difference between these quantities, e.g., $\gamma(\text{WS})$ and $\gamma(\text{den})$, are not so large as in the case of the wobbling motion for the triaxial superdeformed nuclei, they are still sizable and one has to be careful for discussing the triaxial deformation.

One of the interesting quantities studied in part I and also in Ref. [17] is the expectation value of the angular-momentum vector in the body-fixed frame specified by the mean-field, from which the projection is performed. Following the previous work [17], we define the expectation value of each component of the angular-momentum vector in the intrinsic frame for the projected eigenstate α in the following way,

$$(\!(J_i^2)\!)_\alpha \equiv \sum_{KK'} f^{I*}_{K,\alpha}\, \langle IK|J_i^2|IK'\rangle\, f^I_{K',\alpha}, \tag{6}$$

where the index $i = x,y,z$ denotes the axis specified by the deformed mean-field wave function $|\Phi\rangle$, and the $(f^I_{K,\alpha})$ are the properly orthonormalized amplitudes [13], which are defined with the help of the square-root matrix of the norm kernel by

$$f^I_{K,\alpha} = \sum_{K'} (\sqrt{\mathcal{N}^I})_{K,K'}\, g^I_{K',\alpha}. \tag{7}$$

Needless to say, the purely algebraic quantity $\langle IK|J_i^2|IK'\rangle$, e.g., $\langle IK|J_z^2|IK'\rangle = \delta_{KK'}K^2$, should be calculated in the intrinsic frame with $[J_x,J_y] = -i\hbar J_z$ etc. The microscopic geometrical information is contained in the amplitude $f^I_{K,\alpha}$. A more microscopic definition by using the mean-field wave function is necessary to obtain the neutron and proton contributions separately; they are evaluated by ($\tau = \text{n,p}$)

$$\langle\!\langle J_i^{(\tau)2}\rangle\!\rangle_\alpha \equiv \text{Re}\left[\sum_{KK'} g^{I*}_{K,\alpha}\, \langle\Phi|J_i^{(\tau)2}\hat{P}^I_{KK'}|\Phi\rangle\, g^I_{K',\alpha}\right], \tag{8}$$

which are shown to be consistent with the definition of the total expectation value in Eq. (6); i.e., $\langle\!\langle J_i^{(\text{n})2}\rangle\!\rangle_\alpha + \langle\!\langle J_i^{(\text{p})2}\rangle\!\rangle_\alpha \approx (\!(J_i^2)\!)_\alpha$ in a very good approximation, see the discussion in the Appendix of Ref. [17].

III. APPLICATION TO A CHIRAL DOUBLET BAND

The possible existence of chiral doublet bands was first pointed out by Frauendorf and Meng in Ref. [10], and has been explored experimentally since then; see, e.g., Refs. [26,27]. This interesting rotational motion is characteristic for triaxially deformed nuclei. As it was already discussed in part I of the study of nuclear wobbling motion, there are three distinct directions in the body-fixed frame of triaxially deformed nucleus. In the present work, we choose the intrinsic coordinate system that satisfies $\langle x^2\rangle < \langle y^2\rangle < \langle z^2\rangle$; namely, $0 < \gamma < 60^\circ$, and the short, medium, and long axes are x, y, and z axes, respectively. If there are three different kinds of angular-momentum vectors, which favor aligning their vectors along these three principal axes, the three vectors are aplanar in the intrinsic frame. In such a situation, the symmetry of the handedness is broken; i.e., whether these three angular-momentum vectors are right handed or left handed in the xyz intrinsic coordinate is chosen by the self-consistent mean field. Just as in the case of the parity doublet, two almost degenerate $\Delta I = 1$ rotational bands are expected as different linear combinations of the right- and left-handed states, which appear as the chiral doublet bands, see Sec. III A for details.

A prototype example, which was considered in Ref. [10] and in Ref. [12] is the odd-odd nucleus with an odd proton sitting in the high-j particlelike orbit and an odd neutron in the high-j holelike orbit (or vice versa). The high-j particlelike orbit tends to align its angular-momentum vector along the short (x) axis, while the high-j holelike orbit tends to align along the long (z) axis. Moreover, the collective angular momentum prefers to align to the axis with the largest moment of inertia, which is the medium (y) axis for the irrotational-like moments of inertia. Thus an aplanar angular-momentum geometry, i.e., chiral geometry, is expected to appear at the critical spin I_c Below I_c the collective angular momentum lies in the xz plane, see discussion of transverse wobbling [8]. In the present work we study the nucleus ^{128}Cs, in which the odd proton (neutron) occupies the quasiparticle state whose main component is particlelike (holelike) $h_{11/2}$ orbit, and discuss how the chiral geometry comes about. Especially, it is shown that the ideal situation considered in Ref. [12] is indeed realized in our microscopic calculations. In order to demonstrate that the appearance of such an ideal chiral doublet band is not very rare in the calculation, we also briefly discuss another example, ^{104}Rh, in which the odd proton (neutron) occupies the quasiparticle state whose main component is holelike $g_{9/2}$ (particlelike $h_{11/2}$) orbit.

In the following we investigate the chiral doublet bands by the fully microscopic framework of the angular-momentum-projection approach in contrast to the original work [10,12], where the macroscopic model of the triaxial rotor coupled to a particle and a hole is employed. The calculational procedure is the same as in part I. The calculations are performed within the isotropic harmonic oscillator basis and the basis states are truncated up to the maximum oscillator shells, $N_\mathrm{osc}^\mathrm{max} = 12$. As it was explained in detail in part I the monopole-type pairing force strengths are determined to reproduce the even-odd mass differences for the neighboring even-even nuclei, and the average of those is adopted for the odd-odd nucleus. In the present calculation the average pairing gaps for both neutrons and protons are calculated self-consistently using the strengths thus determined. Since we do not intend to reproduce the experimental data but perform explorational calculations, we arbitrarily choose an appropriate value for the deformation parameter β_2, and $\beta_4 = 0.0$ for simplicity, to obtain an ideal chiral geometry. As for the triaxial deformation $\gamma(\mathrm{WS}) = 30^\circ$ is adopted for the Woods-Saxon mean field.

A. Chiral geometry and selection rules for transition rates

Before showing the result of our angular-momentum-projection calculation, we briefly discuss how the chiral geometry is realized and what is expected for it according to Refs. [10,12]; see also the review articles [4,8,11]. In the simple classical model, where a particle and a hole angular momenta, j_p and j_h, align along the short (x) axis and the long (z) axis, respectively, the trajectory of the angular-momentum vector (J_x, J_y, J_z) is given by the intersection of the sphere and the shifted ellipsoid, which are described by the equations,

$$\begin{aligned} &J_x^2 + J_y^2 + J_z^2 = I(I+1), \\ &\frac{(J_x - j_\mathrm{p})^2}{2\mathcal{J}_x} + \frac{J_y^2}{2\mathcal{J}_y} + \frac{(J_z - j_\mathrm{h})^2}{2\mathcal{J}_z} = E, \end{aligned} \tag{9}$$

representing the angular-momentum conservation, I, and the rotor model energy, E, respectively. The quantities, $\mathcal{J}_x$, $\mathcal{J}_y$, and $\mathcal{J}_z$, are the moments of inertia of the core nucleus in the body-fixed frame, and it is assumed that the medium axis has the largest inertia, i.e., $\mathcal{J}_y > \mathcal{J}_x, \mathcal{J}_z$. At low spins the trajectory of the lowest-energy state is mainly confined in the xz principal plane, $J_x \approx j_\mathrm{p}$, $J_z \approx j_\mathrm{h}$, and $J_y \approx 0$, and in the first excited state the angular-momentum vector vibrates with respect to this plane, i.e., the so-called chiral vibration [26]. This chiral vibrational excitation has been studied microscopically by the quasiparticle random-phase approximation in Ref. [28].

When the spin increases and exceeds the critical spin [29],

$$I_\mathrm{c} = \left[\left(\frac{j_\mathrm{p}\mathcal{J}_y}{\mathcal{J}_y - \mathcal{J}_x}\right)^2 + \left(\frac{j_\mathrm{h}\mathcal{J}_y}{\mathcal{J}_y - \mathcal{J}_z}\right)^2\right]^{1/2}, \tag{10}$$

the chiral symmetry is broken in the yrast states; i.e., the aplanar angular-momentum geometry is realized giving the lowest two degenerate solutions, the right-handed (e.g., $J_y > 0$), and the left-handed (e.g., $J_y < 0$) ones, which we denote by $|r\rangle$ and $|l\rangle$, respectively. They are related by $|l\rangle = \mathcal{T}\hat{R}_y(\pi)|r\rangle$, where the operation $\mathcal{T}$ is the time-reversal transformation and $\hat{R}_y(\pi)$ is the π rotation about the y axis. The mean-field solution, which shows the aplanar chiral geometry, was obtained for the first time in Ref. [30] by the microscopic framework of shell-correction tilted axis cranking approach. With the same approach, the transition to the chiral geometry and its critical spin value were investigated from the microscopic view point in Ref. [31] in comparison with the experimental data.

There is tunneling effect between the two solutions, $|r\rangle$ and $|l\rangle$, and the quantum mechanical eigenstates are obtained by the linear combinations,

$$|+\rangle = \frac{1}{\sqrt{2}}(|r\rangle + |l\rangle), \quad |-\rangle = \frac{i}{\sqrt{2}}(|r\rangle - |l\rangle), \tag{11}$$

which are interpreted as the chiral doublet states just like the parity doublet states. Note that the partner states in Eq. (11) are constructed for each spin value, …, $I-1, I, I+1$, …. Now let us consider the electromagnetic transition rates such as $E2$ and $M1$. Since the photon with these low multipolarities cannot

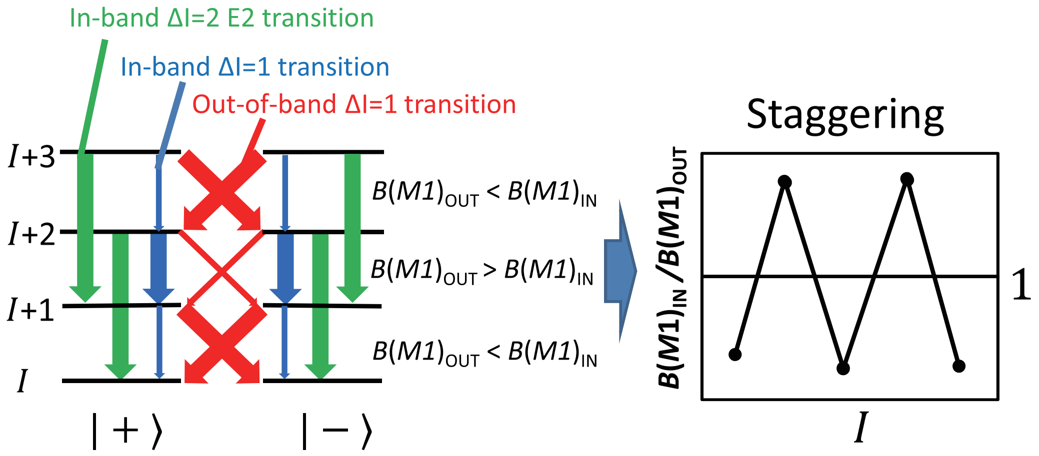

FIG. 1. Schematic figure representing the selection rules of the electromagnetic transitions for the ideal chiral geometry considered in Ref. [12], where the thick (thin) arrow denotes the large (small) transition rate.

turn the angular-momentum vector from the right- to the left-hand position, the overlap $\langle l|\widehat{\mathcal{M}}|r\rangle$ of the transition operator $\widehat{\mathcal{M}}$ is essentially vanishing after the static chiral geometry is realized. Thus these transition rates satisfy the selection rules,

$$\begin{aligned} B(\mathcal{M};+\rightarrow+) &\approx B(\mathcal{M};-\rightarrow-),\\ B(\mathcal{M};-\rightarrow+) &\approx B(\mathcal{M};+\rightarrow-). \end{aligned} \tag{12}$$

Namely, both the in-band transitions and the out-of-band for the pair of the doublet bands are the same.

In Ref. [12] an interesting typical case is considered, which shows especially characteristic properties for the $E2$ and $M1$ transition rates, when the chiral symmetry is broken. Namely, the system is invariant with respect to the combined operation of the $\pi/2$ rotation about the medium (y) axis and an exchange of the valence neutron and proton; this operation is called $\hat{A}$ hereafter, and the eigenstates are classified by the eigenvalues ±1 of $\hat{A}$. Within the simple model in Eq. (9) the system is $\hat{A}$ invariant if the moments of inertia satisfy the condition, $\mathcal{J}_x = \mathcal{J}_z$ and the valence neutron and proton sit in the same high-j orbit, because the $\pi/2$ rotation about the y axis interchanges the x and z axes and at the same time the exchange of valence neutron and proton interchanges the particle and hole alignments $j_{\rm p}$ and $j_{\rm h}$. Considering that the contribution of the valence neutron and proton is almost negligible for the $E2$ operator and that the $M1$ operator has approximate isovector character, it has been shown that these transitions are almost prohibited between the states with same eigenvalue of $\hat{A}$. Moreover, chirality requires that the partner states in Eq. (11) at a given spin have different eigenvalues of $\hat{A}$, because the exchange between the valence neutron and proton while keeping the direction of the rotor angular momentum changes the right- into left-handed states. Taking into account the considerations on top of Eq. (12), the selection rules for the $E2$ and $M1$ transition rates inside and/or between the chiral doublet bands can be summarized in Fig. 1; see Ref. [12] for more detailed discussions. An especially interesting property is seen in the $\Delta I = 1$ $E2$ and $M1$ transitions; the large in-band and small out-of-band transitions and the small in-band and large out-of-band transitions alternate with spin, which can be more clearly observed for the ratio of in-band and out-of-band transitions, e.g., $B(M1)_{\rm in}/B(M1)_{\rm out}$, as it is depicted schematically in the right part of Fig. 1.

In the following we will show that the ideal chiral geometry considered in Ref. [12] is indeed realized in our angular-momentum-projection calculation. This is nontrivial because we do not introduce any kind of rotor and/or valence nucleons explicitly in our fully microscopic framework. However, it is instructive to see moments of inertia of the even-even core nuclei; i.e., ^{128}Xe for the odd-odd nucleus ^{128}Cs with an odd proton particle and an odd neutron hole, and ^{104}Pd for the odd-odd nucleus ^{104}Rh with an odd neutron particle and an odd proton hole. Although we do not explicitly use the three moments of inertia of the principal axes in our framework, their values are of interest. They can be estimated by the cranking procedure; $\mathcal{J}_i = \lim_{\omega_i\to0}\langle J_i\rangle/\omega_i$, where ω_i is the cranking frequency about the ith axis ($i = x,y,z$) of the intrinsic frame. Figures 2 and 3 display the calculated cranking moments of inertia for ^{128}Xe and ^{104}Pd, respectively, as functions of the triaxiality parameter, γ(WS), for the Woods-Saxon potential. As it has been discussed for the wobbling motion in part I, the different definitions of the triaxiality parameter give considerably different values [25]. Therefore, we show the same quantities as functions of the triaxiality parameter, γ(den), for the density distribution defined in Eq. (5), although the differences are not so large as in the case of the triaxial superdeformed states in part I. It should be mentioned that the used mean-field parameters other than the triaxiality are those employed for the analysis of the chiral doublet bands for ^{128}Cs and ^{104}Rh. Therefore the calculated moments of inertia may not be very realistic for ^{128}Xe and ^{104}Pd nuclei themselves. The dependence of three moments of inertia on γ(den) resembles that of irrotational flow; see, e.g., Fig. 1 of part I. However, the relative values are considerably different; at $\gamma = 30^\circ$ $\mathcal{J}_y$ is larger than $\mathcal{J}_x = \mathcal{J}_z$ by a factor 4 for the irrotational flow, while the factor is 2.4–2.6 for the microscopic ones in Figs. 2 and 3. This result is similar to the triaxial superdeformed state in ^{163}Lu studied in part I. We adopt the value $\gamma(\mathrm{WS}) = 30^\circ$ for the analysis, and it can be seen that the necessary condition, $\mathcal{J}_y > \mathcal{J}_x \approx \mathcal{J}_z$, is approximately satisfied in both ^{128}Cs and ^{104}Rh. With these cranking moments of inertia at $\gamma(\mathrm{WS}) = 30^\circ$

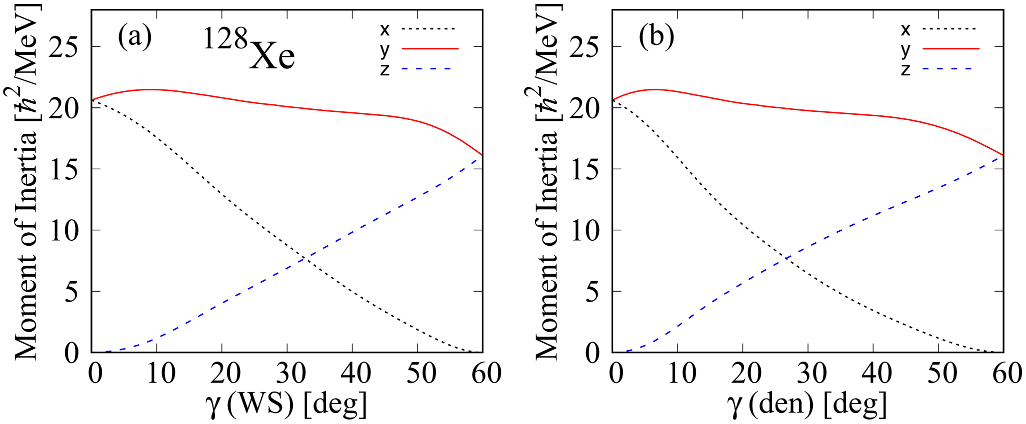

FIG. 2. Cranking moments of inertia of the three intrinsic axes, x, y, and z, which are the short, medium, and long axes, (denoted by dotted, solid, and dashed lines, respectively) as functions of the triaxiality parameter γ for the even-even core nucleus ^{128}Xe of ^{128}Cs. The deformation parameters are $\beta_2 = 0.30, \beta_4 = 0.0$ and the pairing gaps are $\Delta_\mathrm{n} = 0.85$ MeV and $\Delta_\mathrm{p} = 1.07$ MeV, which are are employed for the study of chirality in ^{128}Cs. The γ parameter of the Woods-Saxon potential is utilized in (a) and that of the density distribution, Eq. (5), in (b).

and assuming full alignments for the $h_{11/2}$ and $g_{9/2}$ orbits, the critical angular momentum in Eq. (10) can be estimated to $I_\mathrm{c} \approx 12.9$ for ^{128}Cs and $I_\mathrm{c} \approx 11.8$ for ^{104}Rh.

B. Chiral doublet band in ^{128}Cs

In the course of our investigation we have found that it is difficult to obtain the doublet bands if the mean field is cranked with finite rotational frequencies. Therefore, we do not crank the mean field or just try to make infinitesimal cranking [17] with 10 keV frequencies about three principal axes as was studied in part I. If the mean field is constructed without cranking there is an ambiguity related to the fact that the single-particle states are doubly degenerate (i.e., the Kramers degeneracy), which was already discussed in part I for the odd nucleus ^{163}Lu. These doubly degenerate states are usually classified by the signature, which is the symmetry with respect to the π rotation about one of the intrinsic coordinate axes. We choose the x axis and classify the single-particle orbits by $\hat{R}_x(\pi)$; namely a favored signature state α and its conjugate unfavored state $\bar{\alpha} = -\alpha$. In the case of odd nucleus there is no ambiguity, because the mean-field state with an odd particle in the $\bar{\alpha}$ state is obtained from the mean-field state with an odd particle in the α state by the rotation $\hat{R}_x(\pi)$, and therefore the result of the angular-momentum projection from these two states is exactly the same. For an odd-odd nucleus, however, there are four possible configurations for occupying the odd neutron and odd proton; i.e.,

$$\text{(i)}\ (\alpha_\nu,\alpha_\pi),\quad \text{(ii)}\ (\bar{\alpha}_\nu,\alpha_\pi),\quad \text{(iii)}\ (\alpha_\nu,\bar{\alpha}_\pi),\quad \text{(iv)}\ (\bar{\alpha}_\nu,\bar{\alpha}_\pi). \tag{13}$$

Among them the configuration (iv) is obtained from (i) by $\hat{R}_x(\pi)$, and (iii) from (ii) by $\hat{R}_x(\pi)$, but the configurations (i) and (ii) are independent for the angular-momentum projection calculation. We have numerically confirmed this fact; i.e., the result of projection from the blocked configuration (iv) is exactly the same as that from (i), and the result from (iii) is the same as that from (ii). However, the results of projection from (i) and from (ii) are different, although the differences are found to be very small. One possible way to get rid of the ambiguity is to mix these two independent configurations (i)

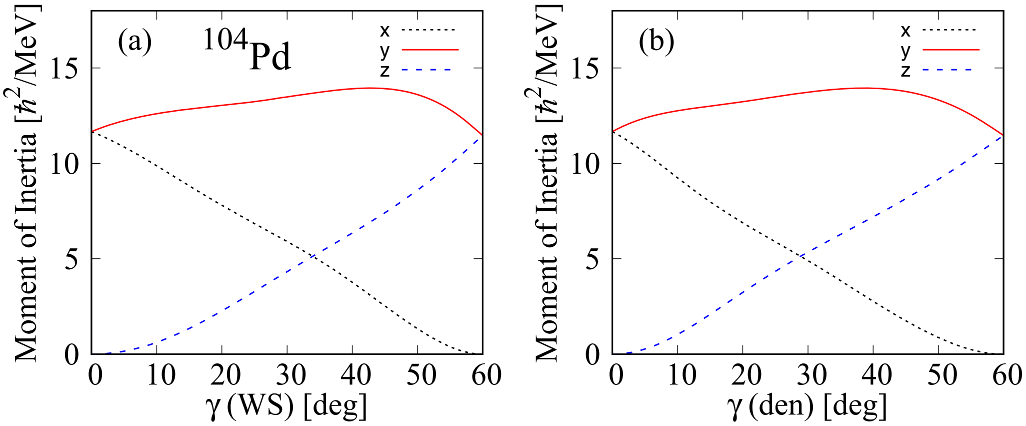

FIG. 3. The same as Fig. 2 but for the even-even core nucleus ^{104}Pd of ^{104}Rh. The deformation parameters are $\beta_2 = 0.25, \beta_4 = 0.0$ and the pairing gaps are $\Delta_\mathrm{n} = 0.95$ MeV and $\Delta_\mathrm{p} = 0.76$ MeV, which are employed for the study of chirality in ^{104}Rh.

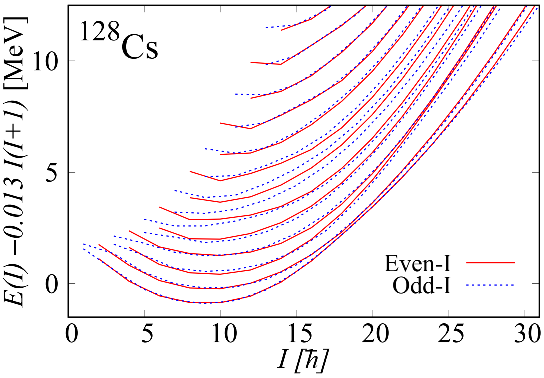

FIG. 4. Energy spectrum for ^{128}Cs calculated by the angular-momentum-projection method from the noncranked mean-field with the configuration (i) in Eq. (13). A rigid-rotor reference energy $0.013\,I(I+1)$ MeV is subtracted.

and (ii) in Eq. (13). We will discuss this point in the following. Practically, we use extremely small cranking frequency $\omega_x = 10^{-10}$ MeV/$\hbar$ and block the lowest quasiparticle state to generate the configuration α and block the second lowest state for the configuration $\bar{\alpha}$. In the following study of ^{128}Cs the blocking of the negative-parity quasiparticle-state originating from the $h_{11/2}$ orbit has been done for both neutron and proton.

The ideal chiral geometry for doublet band does not always appear in the calculation; we need to choose proper deformation parameter. We found that it appears at the deformation parameter $\beta_2 = 0.30$ without hexadecapole deformation; thus we have chosen $\beta_2 = 0.30$, $\beta_4 = 0.0$, and $\gamma = 30^\circ$ for the Woods-Saxon mean field in the following investigation of the chiral doublet band in ^{128}Cs. Note that $\gamma = \gamma(\mathrm{WS}) = 30^\circ$ corresponds to $\gamma(\mathrm{den}) = 24.0^\circ$ in this case. Then, the average pairing gaps calculated self-consistently are $\Delta_{\mathrm{n}} = 0.85$ MeV and $\Delta_{\mathrm{p}} = 1.07$ MeV for neutrons and protons, respectively. It should be mentioned that the adopted value, $\beta_2 = 0.30$, is considerably larger than the ordinary used value, $\beta_2 \approx 0.15$–0.20, in the nuclear region around ^{128}Cs. The resultant rotational spectrum is displayed in Fig. 4, where the angular-momentum projection is performed from the noncranked mean field with configuration (i) in Eq. (13). We have done the same calculation with configuration (ii), but the result is very similar and is not shown. In this and the following figures the even-I and odd-I sequences of the band are connected by the solid and dashed lines, respectively, and a rigid-rotor reference energy $0.013\,I(I+1)$ MeV is subtracted to see more clearly the degeneracy of the bands. This reference energy is selected such that the experimentally observed yrast band is almost flat; see Fig. 5 below. At first sight the excitation spectrum of the multiple-band structure is similar to the wobbling bands in ^{163}Lu studied in part I. However, the yrast wobbling band in ^{163}Lu has the spin values $I-1/2$ being even, and the first excited band has the spin values $I-1/2$ being odd, etc.; i.e., the bands are composed of the $\Delta I = 2$ states and the signature of the multiple wobbling band alternates with increasing energy. In the present case of the multiple bands in ^{128}Cs, the even-I and odd-I bands are almost degenerate and form $\Delta I = 1$ rotational bands. This is because the odd proton aligns its angular-momentum vector along the short (x) axis, while the odd neutron hole aligns its angular-momentum vector along the long (z) axis, and consequently the signature symmetry is strongly broken already at low spins. This is confirmed later by looking at the expectation values of the intrinsic angular-momentum vector in Fig. 6 below. What is important for the spectrum of ^{128}Cs in Fig. 4 is that the energies of the lowest (yrast) and the second lowest (yrare) $\Delta I = 1$ bands become very close in the spin range, $15 \lesssim I \lesssim 25$, which can be well interpreted as the chiral doublet band [10]. The calculated minimum energy difference between the two bands is about 120 keV at $I = 18$. The estimated critical spin $I_{\mathrm{c}} \approx 13$ in Sec. III A is slightly smaller than the spin where the two bands become almost degenerate.

There are two possible configurations for the odd-odd nucleus, those of (i) and (ii) in Eq. (13). Although the resultant spectra obtained from the two configurations are rather similar, we have performed the projected configuration-mixing by including these two configurations in order to obtain the unambiguous result, which is shown in the left panel of Fig. 5. Comparing with the result of Fig. 4, the higher-lying spectrum changes considerably; especially the excitation energies become lower and the level density of the excited bands is higher than those without configuration mixing. However, it should be stressed that the yrast and the yrare bands, which are almost degenerate and so interpreted as chiral doublet bands, are almost the same as without configuration mixing in Fig. 4. However, the agreement with the experimental data is not very good as seen in the right panel of Fig. 5. The calculated bands become degenerate at about $I \approx 15$, while experimentally two bands come together already at $I \approx 11$. Moreover, the slope of the bands is too steep in the calculated bands; namely the moments of inertia are too small compared with the experimental data, which is similar to the calculation of the wobbling band in ^{163}Lu studied in part I.

As it has been pointed out in Ref. [17] infinitesimal cranking quite often improves the calculated moments of inertia. Therefore, we have tried to apply it also to the present case of ^{128}Cs with frequencies $\omega_x = \omega_y = \omega_z = 0.01$ MeV/$\hbar$, where the projection is performed from the single configuration of the infinitesimally cranked mean-field state that is composed of the lowest-energy quasiparticle state for both the odd neutron and proton being blocked. We have found that the result of calculation is very similar to that of mixing the two configurations in Fig. 5, and it is not shown. Namely, the moments of inertia of calculated rotational bands are not improved in this particular case. This result indicates that the time-odd components of the wave function induced by the infinitesimal cranking do not contribute to increase the moments of inertia in this case, although they contain the two different configurations (i) and (ii) in Eq. (13) and their mixing effect.

In order to study the dynamics of the angular-momentum vector, the expectation values of its components in the intrinsic frame, calculated by Eq. (6) for the yrast and yrare bands, are shown in the left panel of Fig. 6. Here the results of the configuration-mixed calculation corresponding to Fig. 5 are displayed but the results are qualitatively similar for other cases. As it is shown in the left panel, all the three components

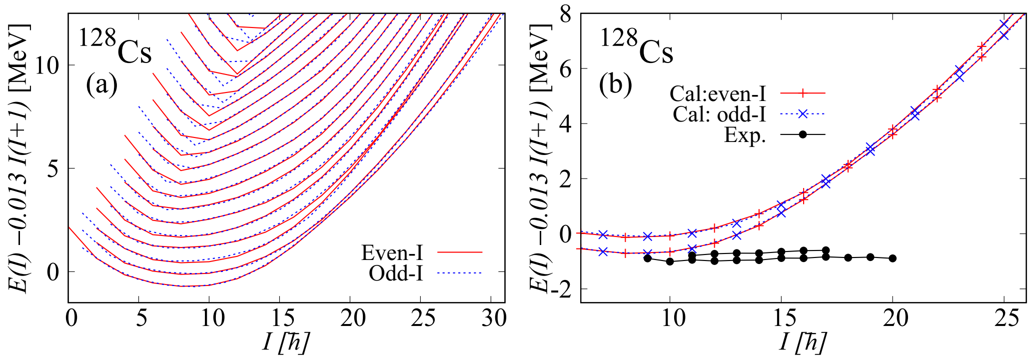

FIG. 5. Left: Energy spectrum for ^{128}Cs calculated by the angular-momentum-projected configuration-mixing method with the two mean-field configurations (i) and (ii) in Eq. (13). Right: Comparison of the calculated and experimental chiral doublet bands in ^{128}Cs. Experimental data are taken from Ref. [27].

of the expectation values of the intrinsic angular-momentum vector are non-negligible. In the lower spin region, $I \lesssim 8$, the dominant components are those along the short (x) and the long (z) axes for the yrast band. As the spin increases, the component of the medium (y) axis, which is the axis with the largest moment of inertia of the core nucleus (see Fig. 2) quickly increases. In the spin range $15 \lesssim I \lesssim 25$ the yrast and yrare have nearly the same geometries, which is characteristic for the chiral regime. The largest component of the angular-momentum vector changes from being along the x axis to along the y axis at $I \approx 18$, which roughly corresponds to the critical angular-momentum of the appearance of the chiral doublet band in Fig. 5. This correspondence between the critical angular momentum and the transition of direction of the angular-momentum vector in the intrinsic frame has also been discussed for the wobbling motion in the ^{163}Lu nucleus studied in part I.

It can be also seen in Fig. 6 that the y component of the yrast band is considerably smaller than that of the yrare band for $I \lesssim 17$, which suggests that the vector of the yrast band stays near the xz principal plane, while the vector of the yrare band goes back and forth with respect to this plane; i.e., the system is in the regime of chiral vibration [26]. Note that the quantities $\langle\langle J_i^2 \rangle\rangle$ in Eq. (6) include such effect of angular-momentum fluctuations. In contrast, the three components of angular-momentum vectors for a pair of the yrast and yrare bands are similar at $I \gtrsim 18$, and form the aplanar configuration, i.e., the system is in the regime of the static chirality; this situation is exactly what is expected for the chiral doublet band to appear. The transition from the regime of the chiral vibration to that of the static chirality occurs gradually. A similar transition expected for the transverse wobbling and related to the direction of the angular-momentum vector in the intrinsic frame has been discussed in part I. How the total angular-momentum vector changes the direction is shown pictorially in Fig. 7 according to the calculation in Fig. 6: The directions of two vectors for the yrast and yrare bands are rather different at $I = 11$; in fact that of the yrare band vibrates with respect to the xz principal plane. At $I = 21$ the two vectors points almost to the same direction, and the yrast and yrare bands can be interpreted as a pair of the doublet band. The x and z components stays almost constants at $I \gtrsim 18$ and the y component becomes dominant at higher spins, $I \gtrsim 30$.

In the chiral regime, the particlelike proton quasiparticle aligns its angular momentum along the x axis and the holelike neutron quasiparticle aligns its angular momentum along the z axis, while the collective angular-momentum vector is mainly along the y axis. To see how neutrons and protons contribute

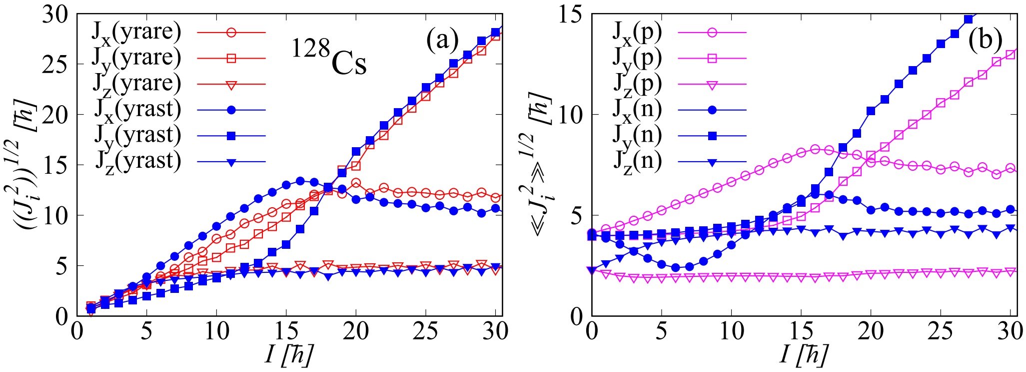

FIG. 6. The calculated expectation values of the angular-momentum vector in the intrinsic frame for the configuration-mixed calculation of ^{128}Cs corresponding to the spectrum in Fig. 5. The left panel shows the expectation values of the total vector for the yrast (filled symbols) and yrare (open symbols) $\Delta I = 1$ bands, while the right panel shows the neutron (filled symbols) and proton (open symbols) contributions in Eq. (8) separately for the yrast band. Note that the x, y, and z axes are the short, medium, and long axes, respectively.

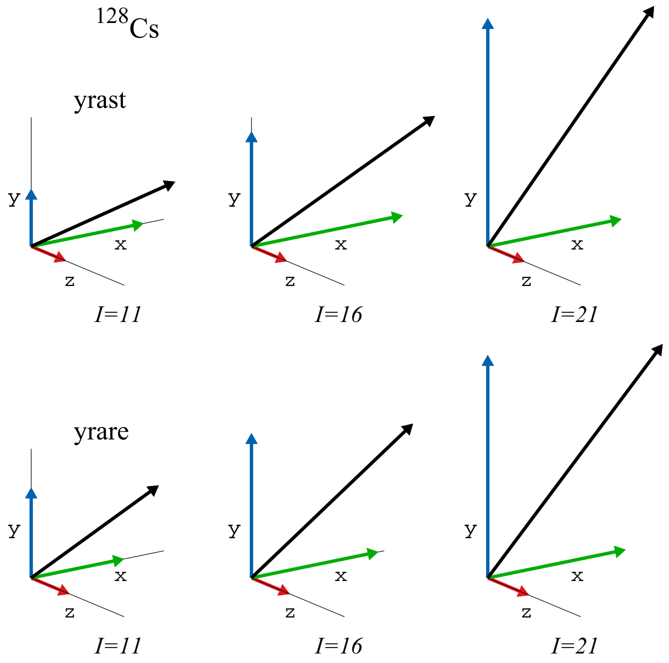

FIG. 7. Angular-momentum vectors in the intrinsic frame for the $I = 11$, 16, and 21 yrast (top) and yrare (bottom) states in ^{128}Cs according to the expectation values shown in Fig. 6.

to the expectation values of the angular-momentum vector, the neutron and proton contributions for the yrast band are depicted separately in the right panel of Fig. 6. The contribution of neutrons or of protons cannot be calculated by Eq. (6); one needs to look into the microscopic wave function explicitly, and Eq. (8) should be used instead. It is seen in the right panel of Fig. 6 that indeed the dominant contribution to the x component comes from proton and that to the z component from neutron, while both neutron and proton contribute to the y component as expected for collective angular momentum. Note that for increase of the x component in the lower spin $I \lesssim 16$, both neutron and proton contribute, which suggests that there is non-negligible amount of collective angular momentum for it. This is consistent with the classical model in Eq. (9). Namely, collective angular momentum increases in the xz plane below the critical spin I_c, while its y component starts to increase after I_c with constant xz components. Thus, the ideal situation of the chiral geometry is realized in this case by our fully microscopic angular-momentum-projection calculation. A similar analysis of the expectation values of angular-momentum vectors has been performed within the particle-rotor model in Refs. [32,33], which allows one to discriminate between collective core and quasiparticle angular-momenta in contrast to our microscopic analysis.

One of the merits of the angular-momentum-projection method is that the electromagnetic transition rates between any eigenstates can be calculated straightforwardly. In the present work, we concentrate on the in-band and out-of-band transitions for the two lowest $\Delta I = 1$ bands, the yrast and the yrare bands, obtained by configuration mixing of the two configurations (i) and (ii) in Eq. (13). The $I \to I-2$ rotational $E2$ transition rates are shown in Fig. 8. The in-band transitions are always large. In fact the large $B(E2: I \to I-2)$ values are used to define each rotational band. The in-band transition rates are similar for the pair of the yrast and yrare bands, where those of the yrare band are slightly larger at lower spins, $I \leqslant 17$, while those of the yrast band are slightly larger at higher spins, $I \geqslant 22$. In contrast, the out-of-band transition probabilities are generally small, although they are non-negligible in $17 \leqslant I \leqslant 23$, where the splitting of the energies of the two bands are smallest and the mixing between them is expected. Note that the out-of-band transitions from the yrare to the yrast at low spins, $I \leqslant 15$, are not so small, while those from the yrast to the yrare are very small, which is characteristic for chiral vibrations. The increasing behavior of the in-band $E2$ transitions results from the change of direction of the angular-momentum vector in the intrinsic frame for the fixed deformation of the mean field. In the semiclassical approximation the $B(E2)$ values are proportional to $|\langle x_j^2 - x_k^2 \rangle|^2$ for the rotation about the ith principal axis (ijk-cyclic), and for rotation about the tilted axis the transition amplitudes are given by the linear combination of these moments $\langle x_j^2 - x_k^2 \rangle$ depending on the angles of the angular-momentum vector (c.f. the formulas in Refs. [34,35]). In the present case, $0 < \gamma < 60^\circ$, the moment $\langle z^2 - x^2 \rangle$ is largest and the maximum value of $B(E2)$ is expected for the rotation about the y axis, which is realized at much higher spins, see the left panel of Fig. 6. This increase of the rotational $B(E2)$ values has been also seen in the particle-rotor model calculation of Ref. [33]. However, the measured rotational $B(E2)$ values [36] do not show such increase with spin; they even slightly decrease at highest spins observed. Moreover, the calculated $B(E2)$ values are about factor two larger than the measured values; this is because the value of β_2 employed in the present study is too large as mentioned previously. Therefore, we do not attempt to make detailed comparison with experimental data except for the $B(M1)_{\rm in}/B(M1)_{\rm out}$ ratio.

The characteristic geometry of the static chirality is reflected in the $\Delta I = 1$ electromagnetic transition rates as it is reviewed in Sec. III A. We show the $I \to I-1$ $E2$ and $M1$ transition rates as functions of spin in Fig. 9 (both in-band and out-of-band transitions). It is clearly seen that the behavior of both $E2$ and $M1$ transitions changes around $I = 16$. The $B(E2)$ and $B(M1)$ for the yrast and yrare bands become similar after the chiral geometry is realized in $I \gtrsim 16$. For $I \lesssim 15$ the in-band transitions are larger than the out-of-band transitions. For $I \gtrsim 16$ the in-band and out-of-band transitions are of similar magnitude, and both of them show the characteristic zigzag pattern. Especially, the in-band (out-of-band) transition rates are prohibitively small at even (odd) spins, and which transition is stronger, the in-band or the out-of-band, changes alternatively as a function of spin. This is exactly what is expected from the prototype model of Ref. [12] (see Fig. 1). As often shown in the experimental data, the $B(M1)/B(E2)$ ratios for the yrast and yrare bands are displayed in a logarithmic scale in the left panel of Fig. 10. Again, the behavior of the ratios changes after the critical spin and clearly shows a regular zigzag pattern, which comes from the $M1$ transitions. As it is discussed in Sec. III A, the clear signature of this ideal scenario

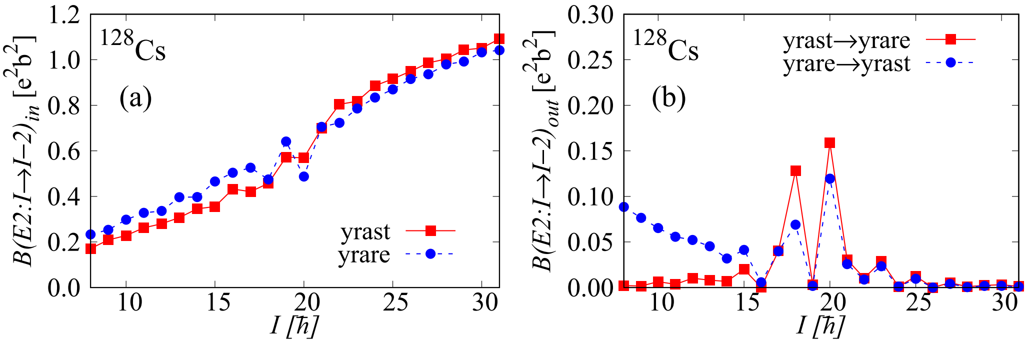

FIG. 8. The calculated $B(E2 : I \to I-2)$ values for the yrast band (solid lines) and the yrare band (dashed lines) as functions of spin in ^{128}Cs. The left and right panels show the in-band and out-of-band values, respectively. Note that the ordinate scale in the right panel is different from that in the left panel. Shown are the results of the configuration-mixed projection calculation corresponding to Fig. 5.

can be seen for the ratio of in-band versus out-of-band $M1$ transitions, which is compared with experimental data [27] in the right panel of Fig. 10. For $I \gtrsim 17$ this ratio alternates values greater than one at odd spin and smaller than one at even spin alternatively, which well corresponds to experimentally observed feature, although the spin range is slightly shifted as expected from the excitation energies in the right panel of Fig. 5. In this way, the result of the present microscopic calculation clearly shows the characteristic behavior of the chiral geometry predicted by the phenomenological model of Ref. [12] not only for the energy spectrum but also for the transition rates.

To see the effect of the triaxial deformation we have done the same calculation using smaller values of γ than 30°: The resultant energy difference between the yrast and yrare bands increases and the amplitude of the zigzag behavior of the $I \to I-1$ $E2$ and $M1$ transitions decreases, while the $I \to I-2$ rotational $E2$ transitions do not essentially change. As an example, we show the result of the $B(M1)/B(E2)$ and $B(M1)_{\rm in}/B(M1)_{\rm out}$ ratios in Fig. 11, which is obtained by the calculation using $\gamma(\text{WS}) = 25^\circ$ and keeping the other parameters unchanged. Note that $\gamma(\text{WS}) = 25^\circ$ corresponds to $\gamma(\text{den}) = 19.3^\circ$. As it is seen in Fig. 2, the moment of inertia $\mathcal{J}_x$ is about factor two larger than $\mathcal{J}_z$ in contrast to the case of $\gamma(\text{WS}) = 30^\circ$ with $\mathcal{J}_x \approx \mathcal{J}_z$, which is the necessary condition for the model of Ref. [12]. The minimum energy difference between the yrast and yrare bands in this case is about 340 keV at $I = 21$, which is about a factor of three larger than that in the case of $\gamma(\text{WS}) = 30^\circ$. As it is clearly seen by comparing Fig. 11 with Fig. 10, the amplitude of the zigzag behavior is reduced by one to two orders of magnitude. Therefore, as it is emphasized in Ref. [12], the $B(M1)_{\rm in}/B(M1)_{\rm out}$ ratio tells

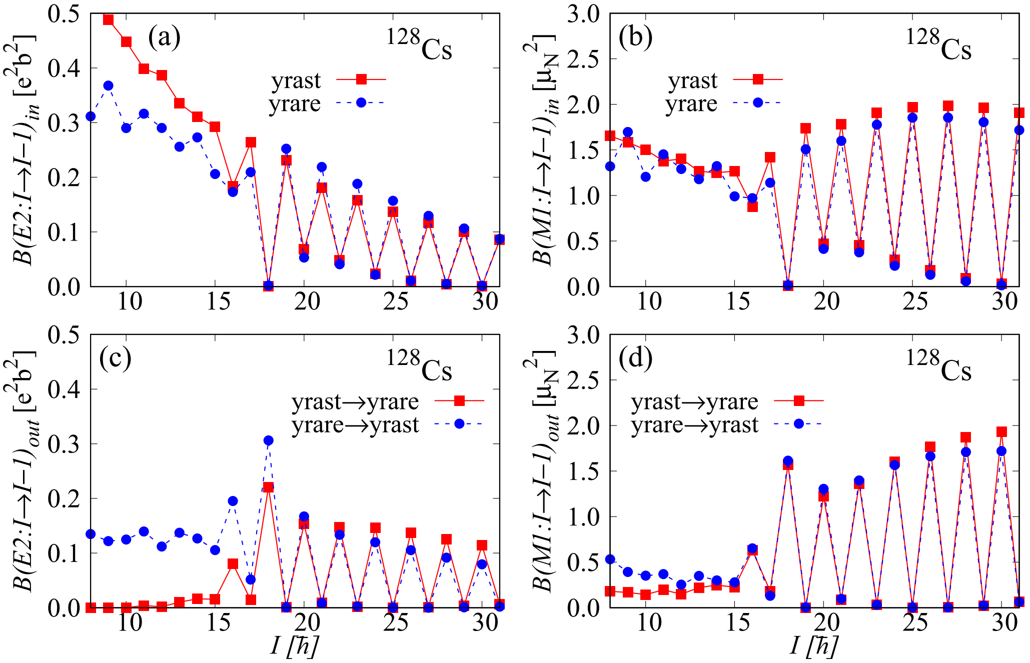

FIG. 9. The calculated $B(E2 : I \to I-1)$ and $B(M1 : I \to I-1)$ values for the yrast band (solid lines) and the yrare band (dashed lines) as functions of spin in ^{128}Cs. The top (bottom) panels show the in-band (out-of-band) transition rates. These are the results of the configuration-mixed projection calculation corresponding to Fig. 5.

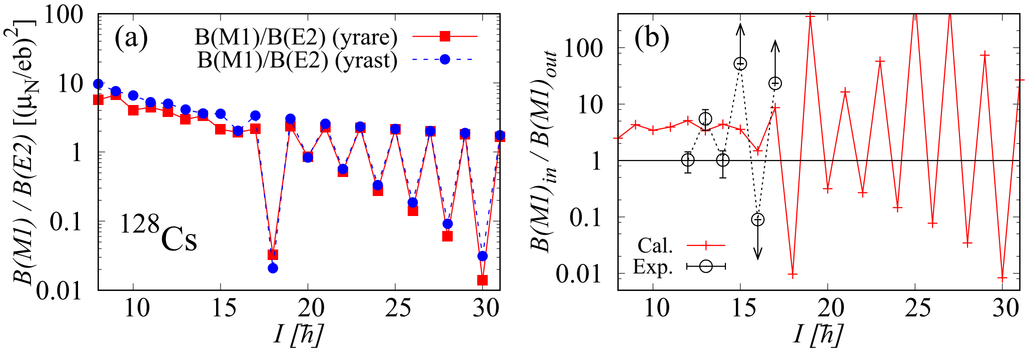

FIG. 10. Left: The calculated $B(M1 : I \to I-1)/B(E2 : I \to I-2)$ ratios inside the yrast band (solid lines) and inside the yrare band (dashed lines) as functions of spin for ^{128}Cs. Right: The ratio of the $I \to I-1$ in-band and out-of-band $M1$ transitions, $B(M1)_{\rm in}/B(M1)_{\rm out}$, where the in-band transitions are those inside the yrare band and the out-of-band transitions are those from the yrare to the yrast band. As for $B(M1)_{\rm in}/B(M1)_{\rm out}$ the experimental data are also included [27]. These are the results of projection with the configuration mixing corresponding to Fig. 5.

how well the situation of the model is realized. These results are consistent with those of the particle-rotor model in Ref. [33], where the results of calculations with several different γ values are presented.

C. Chiral doublet band in ^{104}Rh

As another example of a chiral doublet band in an odd-odd nucleus, we present the result of calculations for ^{104}Rh, where the odd neutron occupies the particlelike negative parity orbit (mainly $h_{11/2}$) and the odd proton occupies the holelike positive parity orbit (mainly $g_{9/2}$). In this case the high-j orbits of the odd neutron and proton are different. The resultant rotational band has negative parity. The calculational procedure is the same as for ^{128}Cs. The adopted deformation parameters are $\beta_2 = 0.25$, $\beta_4 = 0.0$, and $\gamma = 30^\circ$, for which we have found that a chiral doublet band appears in the calculations. Note that $\gamma = \gamma(\mathrm{WS}) = 30^\circ$ corresponds to $\gamma(\mathrm{den}) = 24.9^\circ$ in this case. The average pairing gaps, calculated self-consistently, are $\Delta_{\rm n} = 0.95$ MeV and $\Delta_{\rm p} = 0.76$ MeV for neutrons and protons, respectively. The adopted value, $\beta_2 = 0.25$, is again larger than the commonly used value, $\beta_2 \approx 0.18$–0.23, in the nuclear region around ^{104}Rh. For this nucleus we show only the result of projection from the non-cranked mean-field state constructed by the configuration (i) in Eq. (13) for simplicity; other results are qualitatively similar.

The calculated spectrum is displayed in the left panel of Fig. 12. The rigid-rotor reference energy $0.017\, I(I+1)$ MeV is subtracted to see the details more clearly. Just like the case of ^{128}Cs in Fig. 4, the even-I and odd-I sequences are nearly degenerate indicating the signature symmetry is strongly broken. The lowest two $\Delta I = 1$ bands, which are separated by more than 1 MeV at low spins, quickly approach each other within about $200 - 350$ keV in the spin range $14 \lesssim I \lesssim 20$. The estimated critical spin $I_{\rm c} \approx 12$ in Eq. (10) is slightly smaller than the spin where the two bands become almost degenerate. This behavior rather well corresponds to the observed one [37], although the moments of inertia of these bands are underestimated compared with the experimental data as it is shown in the right panel of Fig. 12. The chiral geometry is confirmed also in this case by the expectation values of the angular-momentum vector in the intrinsic frame, which are depicted in Fig. 13. At the low spins, $I \lesssim 8$, the components of the short (x) and long (z) axes are dominant for the yrast band, while the component of the medium (y) axis quickly grows. All three components give important contributions at the intermediate spin region; see the left panel of Fig. 13. As it is discussed in the case of ^{128}Cs, the y component of the angular-momentum vector for the yrare band is considerably larger than that for the yrast band at $I \lesssim 15$, which indicates that the yrare band can be interpreted as one-phonon excitation of the chiral vibration at this lower spin region. As expected,

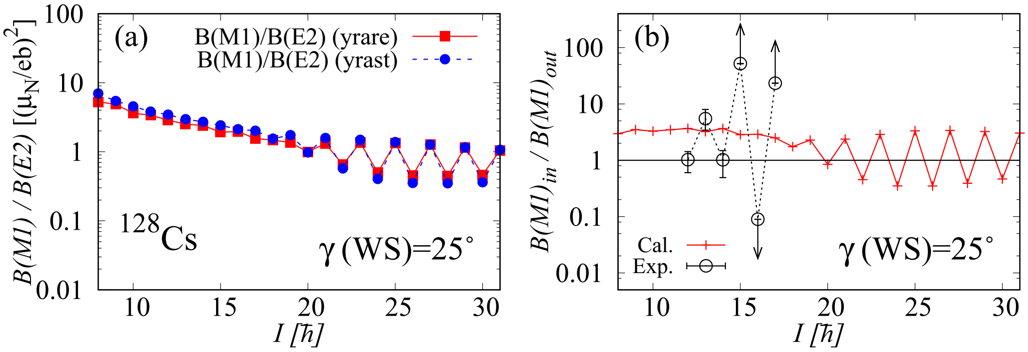

FIG. 11. The same as Fig. 10 but the calculation with using $\gamma(\mathrm{WS}) = 25^\circ$.

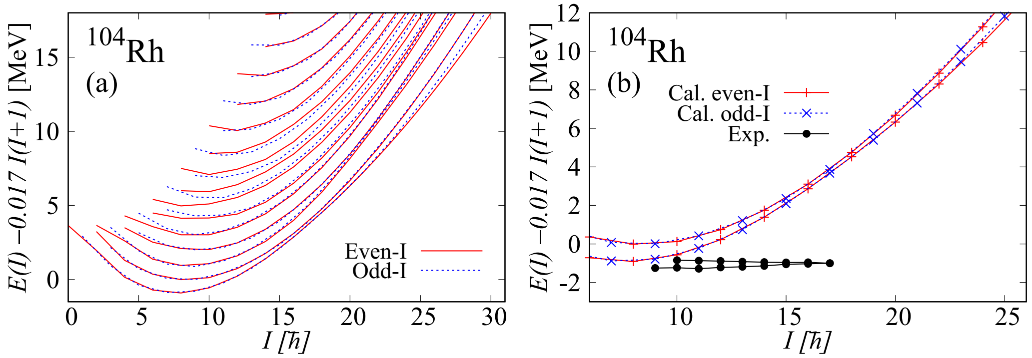

FIG. 12. Left: Energy spectrum for ^{104}Rh calculated by the angular-momentum-projection method from the noncranked mean-field with the configuration (i) in Eq. (13). A rigid-rotor reference energy of 0.017 $I(I+1)$ MeV is subtracted. The lowest fourteen bands for both even-I and odd-I sequences are shown. Right: Comparison of the calculated and experimental chiral doublet bands in ^{104}Rh. Experimental data are taken from Ref. [37].

for $I \gtrsim 16$ the behavior of the angular-momentum vectors indicates that the system is in the regime of the static chirality.

Looking into the right panel of Fig. 13, where the neutron and proton contributions are displayed separately, the main contribution comes from the neutron for the x component and from the proton for the z component, while both neutron and proton coherently contribute to the y component as expected for collective angular momentum. The axis with the largest moment inertia is the y axis as it is seen from the cranking inertias of the core nucleus in Fig. 3. This collective angular-momentum component is very small below I_c and starts to increase at higher spins $I > I_c$. Below I_c, the collective part lies mainly in the xz plane with the x component being more favored as in the case of ^{128}Cs, but neutrons contribute to it more than protons in contrast to ^{128}Cs. This behavior is again consistent with the model in Sec. III A. Thus, the expected transition from the regime of the chiral vibration to that of the static chirality is also confirmed in this case.

The $B(E2)$ and $B(M1)$ values inside the yrast and yrare bands as well between the two bands are also calculated for ^{104}Rh. The $I \to I-2$ stretched $B(E2)$ values are displayed in Fig. 14. It is seen that the in-band values are large and are similar for the yrast and the yrare bands. These rotational transition probabilities increase as functions of spin, which corresponds to the fact that the direction of the angular-momentum vector changes gradually to the medium (y) axis as the spin increases, as it is shown in Fig. 13. The out-of-band transitions are non-negligible for $16 \leqslant I \leqslant 19$, where the difference of energies between the two bands is very small and band mixing is expected. These features are very similar to the case of ^{128}Cs. The $B(E2)$ values seem to be overestimated compared with the experimental data [38], because the deformation parameter $\beta_2 = 0.25$ may be too large.

The calculated $B(E2: I \to I-1)$ and $B(M1: I \to I-1)$ values are shown in Fig. 15 in the same way as in the case of ^{128}Cs. The behavior of both $B(E2)$ and $B(M1)$ as functions of spin changes at around $I \approx 15$; after this spin they exhibit typical zigzag behavior, which is expected after the static chirality is realized. As it is predicted in the prototype model of Ref. [12], the in-band transitions are large when the out-of-band transitions are small and vice versa. In case of ^{104}Rh the in-band (out-of-band) transitions are almost negligible for odd (even) spins, which is opposite to the case of ^{128}Cs. This may be expected because both the particle and hole orbits are mainly $h_{11/2}$ in ^{128}Cs, while the proton hole orbit in ^{104}Rh is mainly $g_{9/2}$: If one $h_{11/2}$ hole is replaced with $g_{g/2}$, the coupled total

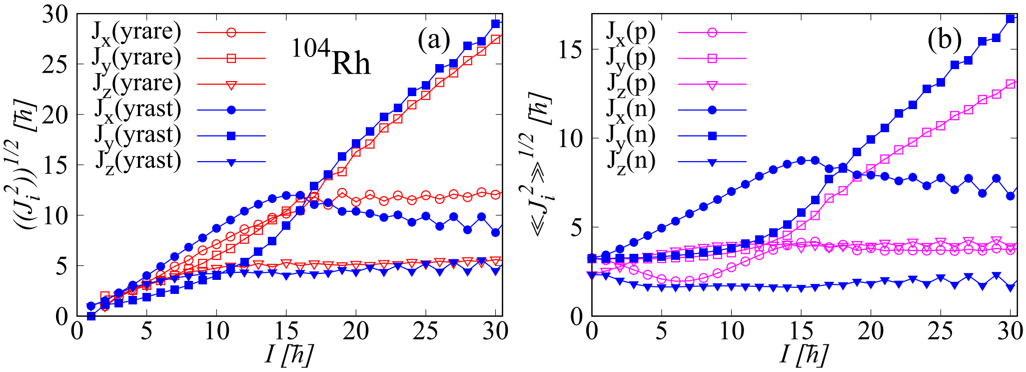

FIG. 13. The calculated expectation values of the angular-momentum vector in the intrinsic frame for the noncranked mean-field of ^{104}Rh corresponding to the spectrum in Fig. 12. The left panel shows the expectation values of the total vector for the yrast (filled symbols) and yrare (open symbols) $\Delta I = 1$ bands, while the right panel shows the neutron (filled symbols) and proton (open symbols) contributions in Eq. (8) separately for the yrast band. Note that the x, y, and z axes are the short, medium, and long axes, respectively.

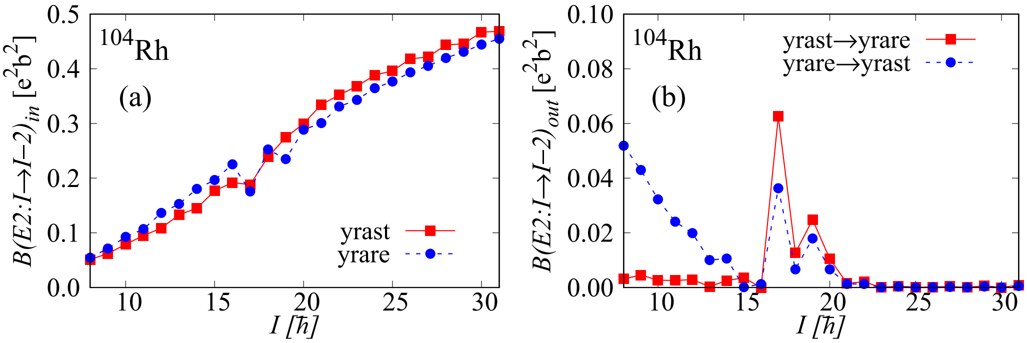

FIG. 14. The calculated $B(E2 : I \to I-2)$ values for the yrast band (solid lines) and the yrare band (dashed lines) as functions of spin in ^{104}Rh. The left and right panels show the in-band and out-of-band transition rates, respectively. Note that the ordinate scale in the right panel is different from that in the left panel. These are the results of projection from the non-cranked lowest configuration (i) in Eq. (13) corresponding to Fig. 12.

spin may be reduced by one unit. Finally, the $B(M1)/B(E2)$ ratio and the in-band versus out-of-band $B(M1)$ ratio are shown in the logarithmic scale in the left and right panels of Fig. 16, respectively. As discussed in the case of ^{128}Cs, The $B(M1)/B(E2)$ ratio changes to the regular zigzag behavior after the chiral geometry is realized, which reflects the behavior of the $B(M1)$ values. The in-band versus out-of-band $B(M1)$ ratio also shows a characteristic pattern, namely it alternates between values greater than one and smaller than one as a function of spin. This is the expected behavior from the model in Ref. [12] (see Fig. 1). However, it should be noted that the neutron-proton symmetry prerequisite in the model of Ref. [12] is not precisely satisfied in the present example, because the high-j orbits of the odd neutron and proton are different. It is interesting that the calculation shows the characteristic selection rules of the model even in this case. In fact, the particle-rotor model calculation with proton $g_{9/2}$ and neutron $h_{11/2}$ orbits in Ref. [39] shows similar zigzag behavior for $B(M1)$ for the neighboring nucleus ^{106}Rh. Although the zigzag behavior of $B(M1)$ are observed in the experimental data [37,38], its amplitude is too large in the present calculation. The observed doublet band may not come as close to the model of Ref. [12] as our calculations.

Finally, we show the results of a calculation using $\gamma = \gamma(\mathrm{WS}) = 25^\circ$ for this nucleus. Note that $\gamma = \gamma(\mathrm{WS}) = 25^\circ$ corresponds to $\gamma(\mathrm{den}) = 20.2^\circ$ in this case. The moment of inertia $\mathcal{J}_x$ is about factor two larger than $\mathcal{J}_z$ (see Fig. 3). Figure 17 depicts the $B(M1)/B(E2)$ and $B(M1)_{\mathrm{in}}/B(M1)_{\mathrm{out}}$ ratios like Fig. 16. Apparently, the magnitude of the oscillation of the $B(M1)$ values are reduced by one to two

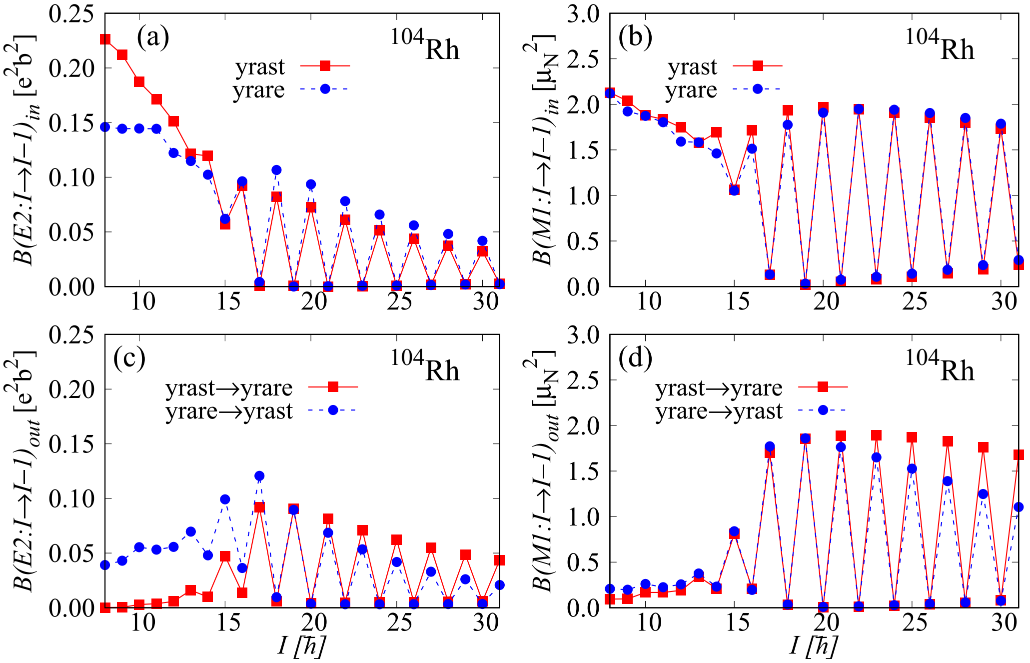

FIG. 15. The calculated $B(E2 : I \to I-1)$ and $B(M1 : I \to I-1)$ values for the yrast band (solid lines) and the yrare band (dashed lines) as functions of spin in ^{104}Rh. The top (bottom) panels show the in-band (out-of-band) transition rates. These are the results of projection from the noncranked lowest configuration (i) in Eq. (13) corresponding to Fig. 12.

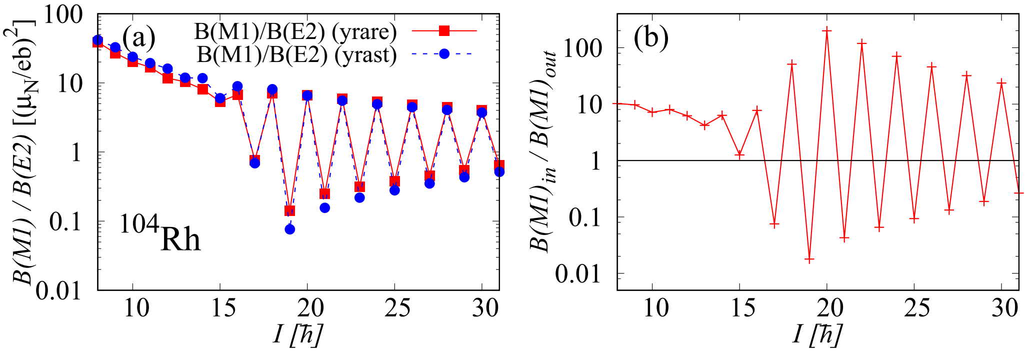

FIG. 16. Left: The calculated $B(M1: I \rightarrow I-1)/B(E2: I \rightarrow I-2)$ ratios inside the yrast band (solid lines) and inside the yrare band (dashed lines) as functions of spin for ^{104}Rh. Right: The ratio of the $I \rightarrow I-1$ in-band and out-of-band $M1$ transitions, $B(M1)_{\rm in}/B(M1)_{\rm out}$, where the in-band transitions are those inside the yrare band and the out-of-band transitions are those from the yrare to the yrast band. These are the results of projection from the noncranked mean-field corresponding to Fig. 12.

orders of magnitude. The out-of-band $B(M1)$ values become smaller than the in-band values, and the center of the oscillations is changed to a value that is considerably larger than one.

IV. SUMMARY

In this series of investigation, we have studied rotational motion that is characteristic for nuclei with triaxial deformation. The basic method we employed is the fully microscopic framework of angular-momentum projection from the mean-field wave function, where the microscopic Hamiltonian is composed of the Woods-Saxon mean-field and the separable schematic interaction. Among various interesting types of rotational motion, we have concentrated on the nuclear wobbling motion and the chiral vibrations and rotations. The former is the subject of part I and the latter is the subject of the present part II in the series.

The nuclear chirality of rotating triaxially deformed nucleus is a relatively new concept and it is expected in odd-odd nuclei as typical examples. We have applied our microscopic framework to the typical cases of two odd-odd nuclei, ^{128}Cs and ^{104}Rh, where the odd proton (neutron) occupies the high-j particlelike orbit and the odd neutron (proton) occupies the high-j holelike orbit in the former (latter) nucleus. The odd nucleons occupying the particlelike and holelike orbits align their angular-momentum vectors along the short and long axes, respectively. Combined with the collective rotation around the medium axis, which has the largest moment of inertia, these three angular-momentum vectors form an aplanar configuration, i.e., the chiral geometry is realized in the body-fixed frame of the triaxial mean field. In such a situation the chiral symmetry between the right- and left-handedness is broken, which is the reason why the chiral doublet band emerges [10]. Adjusting the quadrupole deformation parameter β_2 and fixing the triaxiality parameter at $\gamma(\mathrm{WS}) = 30^\circ$ we are able to obtain the yrast and yrare bands as a chiral doublet by our fully microscopic angular-momentum-projection calculation. By calculating the expectation values of the angular-momentum vector with respect to the three principal axes, it is confirmed that the chiral geometry is realized for the selected examples of ^{128}Cs and ^{104}Rh. However, the moments of inertia of the calculated bands are too small compared with the experimental data. One of the merits of the angular-momentum-projection method is feasibility for calculating the electromagnetic transition probabilities. We have studied the $E2$ and $M1$ transitions between the members of the doublet bands. It is demonstrated that the $I \rightarrow I-1$ transition rates completely change their behavior after the static chirality is reached. Large and small reduced probabilities alternate as functions of spin, and this behavior is out of phase for the in-band and out-of-band transitions. This characteristic feature is in accordance with

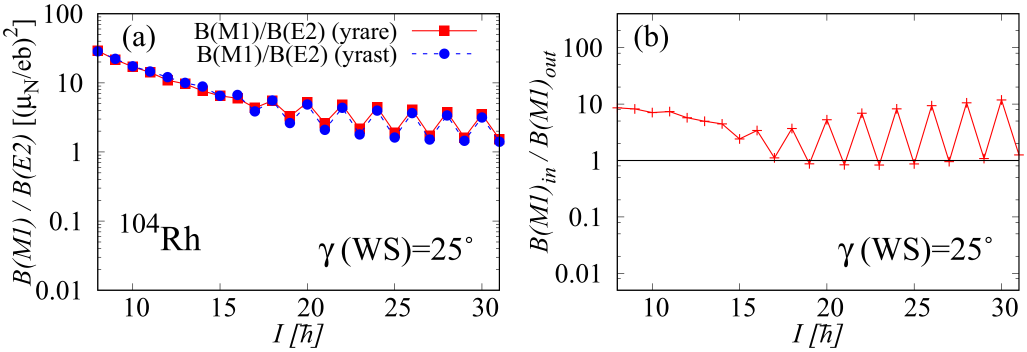

FIG. 17. The same as Fig. 16 but the calculation with using $\gamma(\mathrm{WS}) = 25^\circ$.

the prototype model proposed in Ref. [12], and qualitatively corresponds to the experimental data for both ^{128}Cs and ^{104}Rh.

In this way, we have confirmed that the two interesting types of rotational motion, the wobbling motion and the chiral rotation, which are characteristic for the triaxially deformed nuclei, naturally emerge as results of our fully microscopic angular-momentum-projection calculation. The wobbling bands and chiral doublet bands were originally predicted based on the macroscopic rotor model or the phenomenological particle-rotor coupling model. Considering the fact that the predicted properties by these models are confirmed by our microscopic calculations, the macroscopic rotor model picture is well realized for the triaxially deformed nucleus. It should, however, be noticed that a quantitative description of these rotational bands is not achieved in the present series of work. Further investigation is needed for a quantitative description of the data.

[1] A. Bohr and B. R. Mottelson, *Nuclear Structure*, Vol. II (Benjamin, New York, 1975).

[2] P. Möller, R. Bengtsson, B. G. Carlsson, P. Olivius, and T. Ichikawa, Phys. Rev. Lett. **97**, 162502 (2006).

[3] M. J. A. de Voigt, J. Dudek, and Z. Szymanski, Rev. Mod. Phys. **55**, 949 (1983).

[4] S. Frauendorf, Rev. Mod. Phys. **73**, 463 (2001).

[5] S. C. Pancholi, *Exotic Nuclear Excitations*, Springer Tracts, in Modern Physics 242 (Springer, Berlin, 2011).

[6] S. W. Ødegård, G. B. Hagemann, D. R. Jensen, M. Bergström, B. Herskind, G. Sletten, S. Törmänen, J. N. Wilson, P. O. Tjøm, I. Hamamoto, K. Spohr, H. Hübel, A. Görgen, G. Schönwasser, A. Bracco, S. Leoni, A. Maj, C. M. Petrache, P. Bednarczyk, and D. Curien, Phys. Rev. Lett. **86**, 5866 (2001).

[7] T. Nakatsukasa, K. Matsuyanagi, M. Matsuzaki, and Y. R. Shimizu, Phys. Scr. **91**, 073008 (2016).

[8] S. Frauendorf, Phys. Scr. (to be published).

[9] M. Shimada, Y. Fujioka, S. Tagami, and Y. R. Shimizu, Phys. Rev. C **97**, 024318 (2018).

[10] S. Frauendorf and J. Meng, Nucl. Phys. A **617**, 131 (1997).

[11] K. Starosta and T. Koike, Phys. Scr. **92**, 093002 (2017).

[12] T. Koike, K. Starosta, and I. Hamamoto, Phys. Rev. Lett. **93**, 172502 (2004).

[13] P. Ring and P. Schuck, *The nuclear many-body problem* (Springer, Berlin, 1980).

[14] S. Tagami and Y. R. Shimizu, Prog. Theor. Phys. **127**, 79 (2012).

[15] S. Tagami, Y. R. Shimizu, and J. Dudek, Phys. Rev. C **87**, 054306 (2013).

[16] S. Tagami, Y. R. Shimizu, and J. Dudek, J. Phys. G **42**, 015106 (2015).

[17] S. Tagami and Y. R. Shimizu, Phys. Rev. C **93**, 024323 (2016).

[18] M. Shimada, S. Tagami, and Y. R. Shimizu, Prog. Theor. Exp. Phys. **2015**, 063 (2015).

[19] M. Shimada, S. Tagami, and Y. R. Shimizu, Phys. Rev. C **93**, 044317 (2016).

[20] G. H. Bhat, J. A. Sheikh, and R. Palit, Phys. Lett. B **707**, 250 (2012).

[21] Y. Sun, Phys. Scr. **91**, 043005 (2016).

[22] J. A. Sheikh, G. H. Bhat, W. A. Dar, S. Jehangir, and P. A. Ganai, Phys. Scr. **91**, 063015 (2016).

[23] S. Tagami, M. Shimada, Y. Fujioka, Y. R. Shimizu, and J. Dudek, Phys. Scr. **89**, 054013 (2014).

[24] T. Bengtsson and I. Ragnarsson, Nucl. Phys. A **436**, 14 (1985).

[25] Y. R. Shimizu, T. Shoji, and M. Matsuzaki, Phys. Rev. C **77**, 024319 (2008).

[26] K. Starosta, T. Koike, C. J. Chiara, D. B. Fossan, D. R. LaFosse, A. A. Hecht, C. W. Beausang, M. A. Caprio, J. R. Cooper, R. Krücken, J. R. Novak, N. V. Zamfir, K. E. Zyromski, D. J. Hartley, D. L. Balabanski, J.-y. Zhang, S. Frauendorf, and V. I. Dimitrov, Phys. Rev. Lett. **86**, 971 (2001).

[27] T. Koike, K. Starosta, C. J. Chiara, D. B. Fossan, and D. R. La Fosse, Phys. Rev. C **67**, 044319 (2003).

[28] D. Almehed, F. Dönau, and S. Frauendorf, Phys. Rev. C **83**, 054308 (2011).

[29] P. Olbratowski, J. Dobaczewski, J. Dudek, and W. Płóciennik, Phys. Rev. Lett. **93**, 052501 (2004).

[30] V. I. Dimitrov, S. Frauendorf, and F. Dönau, Phys. Rev. Lett. **84**, 5732 (2000).

[31] S. Zhu, U. Garg, B. K. Nayak, S. S. Ghugre, N. S. Pattabiraman, D. B. Fossan, T. Koike, K. Starosta, C. Vaman, R. V. F. Janssens, R. S. Chakrawarthy, M. Whitehead, A. O. Macchiavelli, and S. Frauendorf, Phys. Rev. Lett. **91**, 132501 (2003).

[32] B. Qi, S. Q. Zhang, J. Meng, S. Y. Wang, and S. Frauendorf, Phys. Lett. B **675**, 175 (2009).

[33] B. Qi, S. Q. Zhang, S. Y. Wang, J. M. Yao, and J. Meng, Phys. Rev. C **79**, 041302(R) (2009).

[34] S. Frauendorf, Nucl. Phys. **557**, 259c (1993).

[35] S. Frauendorf, Nucl. Phys. **677**, 115 (2000).

[36] E. Grodner, J. Srebrny, A. A. Pasternak, I. Zalewska, T. Morek, Ch. Droste, J. Mierzejewski, M. Kowalczyk, J. Kownacki, M. Kisieliński, S. G. Rohoziński, T. Koike, K. Starosta, A. Kordyasz, P. J. Napiorkowski, M. Wolińska-Cichocka, E. Ruchowska, W. Płóciennik, and J. Perkowski, Phys. Rev. Lett. **97**, 172501 (2006).

[37] C. Vaman, D. B. Fossan, T. Koike, K. Starosta, I. Y. Lee, and A. O. Macchiavelli, Phys. Rev. Lett. **92**, 032501 (2004).

[38] T. Suzuki, G. Rainovski, T. Koike, T. Ahn, M. P. Carpenter, A. Costin, M. Danchev, A. Dewald, R. V. F. Janssens, P. Joshi, C. J. Lister, O. Möller, N. Pietralla, T. Shinozuka, J. Timár, R. Wadsworth, C. Vaman, and S. Zhu, Phys. Rev. C **78**, 031302(R) (2008).

[39] P. Joshi *et al.*, Phys. Lett. B **595**, 135 (2004).